

Sensitivity Analysis of Geometrical Parameters to the Flow of Pre-swirl System after Turbine Blade Fracture

Gang Zhao ¹, Tian Qiu ² and Peng Liu ^{2,*}¹ School of Energy and Power Engineering, Beihang University, Beijing 100191, China² Research Institute of Aero-Engine, Beihang University, Beijing 100191, China

* Correspondence: liupeng91@buaa.edu.cn

Abstract: The pre-swirl stator-rotor system is a common and important structure in gas turbines, and its main function is to provide cold air to the turbine blades with a low relative total temperature. Under normal conditions, the boundaries of the system are symmetrical and there is sufficient margin for each blade. However, a fracture of turbine blades can upset this balance, resulting in potentially different cold-air conditions for each blade. Therefore, to ensure the safety of the other blades after a single-blade break, it is necessary to know the cold-air distribution law of the system after a blade fracture. In this paper, the effects of geometric parameters (including pre-swirl angle, α ; the area ratio of nozzles and holes, ξ ; gap ratio, G ; and radius ratio of nozzle and hole, δ) of a pre-swirl stator-rotor system on the mass-flow-rate ratio, η ; total-pressure-loss coefficient, C_p ; discharge coefficient of holes, C_d ; and adiabatic effectiveness, Θ_{ad} , are investigated by numerical simulation with a single blade fractured. The results show that most of the geometric parameter changes do not increase η_{hole_0} . Moreover, measures to increase the influence of pre-swirl nozzles can reduce the influence of blade fracture on mass flow distribution, such as larger α , smaller ξ , and smaller δ . As for C_p , C_d , and Θ_{ad} , they are more sensitive to changes in α and ξ . For the pre-swirl system, to avoid more serious safety problems caused by individual blade fracture, the designer should make every effort to reduce the unevenness of the cold-air distribution. Increasing the effect of the nozzle could serve the aim, but it may increase the volatility of the flow. The pre-swirl nozzle of the leaf grille type is a good option to address flow fluctuations.

Keywords: rotor-stator pre-swirl system; non-axisymmetric boundary conditions; numerical simulation; blade fracture; passive safety design

Citation: Zhao, G.; Qiu, T.; Liu, P. Sensitivity Analysis of Geometrical Parameters to the Flow of Pre-swirl System after Turbine Blade Fracture. *Aerospace* **2022**, *9*, 783. <https://doi.org/10.3390/aerospace9120783>

Academic Editor: Dimitri Mavris

Received: 10 October 2022

Accepted: 25 November 2022

Published: 1 December 2022

Publisher's Note: MDPI stays neutral with regard to jurisdictional claims in published maps and institutional affiliations.



Copyright: © 2022 by the authors. Licensee MDPI, Basel, Switzerland. This article is an open access article distributed under the terms and conditions of the Creative Commons Attribution (CC BY) license (<https://creativecommons.org/licenses/by/4.0/>).

1. Introduction

Pre-swirl systems are generally used in the internal air systems of gas turbines, such as the direct-transfer pre-swirl supply system that supplies cold air to turbine blades. Its function is to reduce the relative total temperature of the cold air and improve the turbine cooling efficiency. Therefore, it plays a crucial role in turbine cooling.

In terms of pre-swirl system design, many recommendations are given in the papers. Lee et al. [1] investigated the influence of edge shape, inclined angle, area ratio, and the number of receiver holes on the discharge coefficient, adiabatic effectiveness, and pressure drop. Their study showed that the pre-swirl system performance increased as the area ratio increased, and under the fixed area ratio, a large number of small-diameter receiver holes showed better performance. The receiver hole edge fillet was the most influential shape parameter in pre-swirl performance. Zhang et al. [2–4] conducted investigations on the flow and heat-transfer characteristics in a radial pre-swirl system with different fillet radiuses, pre-swirl-nozzle angles, and length-to-diameter ratios of nozzles. Zhao et al. [5] also investigated the effect of the pre-swirl angle of the nozzles on an axial pre-swirl system. Paper [6–9] studied the effect of the radial position of the pre-swirl nozzle

on the pre-swirl cooling system, which suggested that a high-radius ratio of pre-swirl nozzle to receiver hole is a benefit to the discharge coefficient and adiabatic effectiveness.

Under normal conditions, the back pressure at the outlet of the pre-swirl system is the same. The cold air from the compressor enters the stator-rotor system through the nozzle, and most of them enter the turbine blades through the receiver hole to control the blade temperature, except for a small portion for sealing. However, when blades fracture in actual work, the channel inside the broken blades is exposed to the low-pressure mainstream, which results in discrepant pressure at the outlet of the receiver holes. Because of the discrepant pressure, a large volume of cold air will rush to the broken blades, reducing the cold air acquired by the normal blades, assuming that the total volume of cold air is constant. A normal blade may potentially fail, due to over-limiting the thermal stress, because the amount of cold air obtained by the normal blade is less than needed. The distribution of cold air will become increasingly uneven as it continues to develop, and may cause a cascade of blades to break. In addition, the probability of blade fracture is around 10^{-5} times per flight hour [10–12], which is above the probability of hazardous occurrences [13] required by FAA AC 33.75. Therefore, the influence of blade fracture on gas turbines must be demonstrated.

Some studies have been conducted for flow with asymmetric boundary conditions. Bein et al. [14,15] explored a lubricating-oil sealing problem in a narrow rotor-stator cavity. At the outlet of the cavity, there is a high-pressure zone and a low-pressure zone, and at a certain pressure lubricating oil is provided at the disk center. Another class of problems is the flow of magnetic fluids in a microchannel under electromagnetic force and pressure coupling [16]. The asymmetric boundary is caused by electromagnetic force. In addition, there is a class of Couette–Poiseuille flow under asymmetric boundaries [17]. The common feature of the above three types of flows is that viscous forces are not negligible and even dominant. However, for the pre-swirl stator-rotor system, the viscous force is not important and inertial force is not negligible in the rotating core. With this problem, Zhao et al. [18] studied the effect of asymmetric outlet boundaries on a simple stator-rotor system employing numerical simulation, but the effect of geometric parameters was neglected.

To fill the research gap in this topic, and also to provide some ideas and basis for the passive safety design of the pre-swirl system, this paper takes a direct-transfer pre-swirl supply system as the object to study the influence of the geometric parameters of the system on the flow dynamic after a single-blade fracture. In particular, the second part describes in detail the computational setup, including the boundary conditions, verification of the mesh and turbulence models, geometric model information, and definition of key parameters. The third part discussed in detail the effects of the geometric parameters (including the pre-swirl angle, α ; area ratio of nozzles and holes, ξ ; gap ratio, G ; and radius ratio of nozzle and hole, δ) of a pre-swirl stator-rotor system on the mass-flow-rate ratio, η ; total-pressure-loss coefficient, C_p ; discharge coefficient of holes, C_d ; and adiabatic effectiveness, Θ_{ad} , of a pre-swirl system with a single blade fractured.

2. Computational Method

2.1. Computational Model

The computational model used in this paper (shown in Figure 1) is simplified from an actual gas turbine, for which a rich experimental study has been carried out at the University of Bath. The experimental conditions cover typical β_p and λ_T in real engines, and the flow structures studied are typical [19]. Please refer to the papers [7,20–23] for detailed experimental settings and measurements, as only key information is described here.

As shown in Figure 1, the air enters the cavity from the discrete nozzles at a low radius, then flows radially outward influenced by centrifugal force, and finally exits through the receiver hole. Both shroud and hub have a sealing gap of 1 mm in width,

which is ignored in the calculation. The geometric parameters of the experimental apparatus are shown in Table 1. This paper focuses on the effect of the geometric parameters on the flow dynamics of the pre-swirl system after a blade fracture. Therefore, based on the original experimental configuration, this paper plans to separately change the pre-swirl angle, area of nozzle, cavity gap, and radial position of the nozzles to investigate the effects of α , ξ , G , and δ on η , C_p , C_d , and Θ_{ad} . Where $\xi = A_{nozzle}/A_{hole}$, $G = s/b$, $\delta = r_p/r_h$. For a representative study, the range of variation is shown in Table 2.

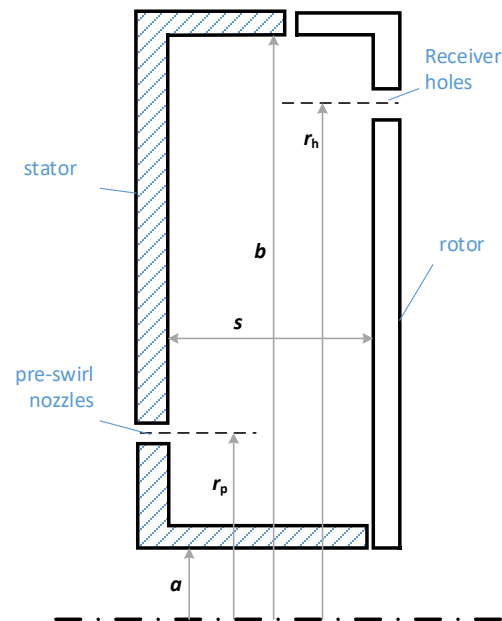


Figure 1. Schematic diagram of the direct-transfer pre-swirl rotor-stator system in this paper.

Table 1. Experimental geometry and operating conditions.

Parameters	Values
Outer disk radius b	0.216 m
Inner radius a	0.145 m
Cavity width s	0.011 m
Pre-swirl-nozzle radius, r_p	0.160 m
Sealing-slot width	0.001 m
Receiver-hole radius, r_h	0.200 m
Receiver-hole diameter	0.008 m
Nozzle diameter	0.0071 m
Pre-swirl angle, α	70°

Table 2. The range of variables.

Parameters	Values
Pre-swirl-nozzle angle, α	0°~70°
The area ratio of nozzles and holes, ξ	0.156~1.225
Gap ratio, G	0.0231~0.0648
Radial location ratio of nozzles and holes, δ	0.8~1.05

The 3D CFD model used for the calculation is divided into two computational domains: a stationary one and a rotational one. The two domains are connected by an interface, which is parallel to the disk (as shown in Figure 2). The medium is a compressible ideal gas and is calculated using the commercial software CFX19 with a physical time step of 2.5×10^{-5} and a convergence criterion of $RSM < 10^{-5}$. There are two steady-state methods

for handling interfaces in CFX, namely Stage and Frozen Rotor [24]. What we study in this paper is an asymmetric boundary condition, and the Frozen Rotor method is more appropriate. The boundary conditions for the calculation are shown in Table 3: the outlet_0 corresponds to the broken blade, so its outlet pressure is lower than that of the other receiver holes. In this paper, the boundary conditions of the pre-swirl system after turbine blade fracture are simulated by the different pressure of the receiver holes. When the outlet pressures of all receiver holes are equal, it means that the turbine blades are not fractured.

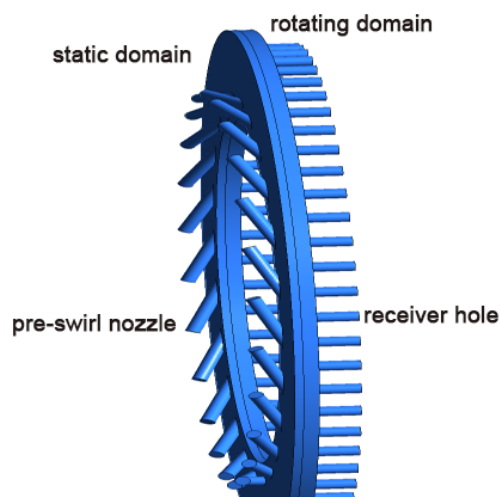


Figure 2. Computational model.

The meshes of the static and rotating domains are all hexahedral, meshed by ICEM. Figure 3 shows the local mesh of the domains. To exclude the influence of mesh, the mesh is periodic. In other words, the static domain is meshed by rotating and coping a 15° mesh 23 times, while the rotating domain is constructed by rotating and coping a 6° mesh 59 times. Therefore, the mesh is axisymmetrical. The thickness of the first layer of the wall boundary layer is 0.002 mm, the growth rate is 1.1, and the Y^+ at the wall surface is less than 1, which only exceeds 1 in a small range near the pre-swirl nozzle and outlets. There are more than 4.5×10^7 grids in total.

Table 3. Boundary conditions.

Parameters	Values
Inlet total temperature, $T_{\text{nozzle,in,stn}}^*$	65.06 °C
Inlet mass flow, m_{nozzle}	0.06 kg/s
Outlet static pressure of hole_0, $P_{\text{hole}_0,\text{out}}$	−571 Pa
Outlet static pressure of hole_i ($i \neq 0$), $P_{\text{hole}_i,\text{out}}$	0 Pa
Reference pressure	101,325 Pa
Rotation speed, Ω	350 rad/s
C_w	13164
Re_ω	7.7×10^5
λ_T	0.26
E [14,18]	0.2



Figure 3. Local grid.

2.2. Computational Validation

There are many turbulence models available in the commercial software CFX. In this paper, four widely used turbulence models are selected for comparison with experiments to obtain the most suitable one for this problem. To save the computational effort, the computational model used in this section is shown in Figure 4. The domain includes a static domain and a rotating domain. The static domain is a sector of 15° with a pre-swirl nozzle, and the rotating domain is 12° with two receiver holes. Figure 5 shows the comparison of static pressure in the static disk between the four turbulence models and the experimental results. It can be seen from the figure that the SST model performs better than the other turbulence models in high-radius regions. Combined with the research of other authors [4,24,25], all the following cases employ the SST turbulence model.

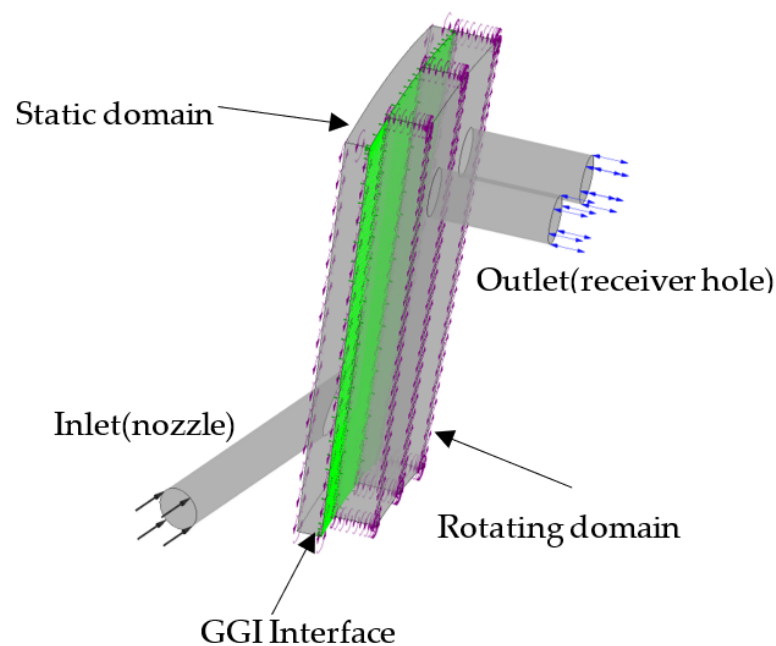


Figure 4. The computational model used in computational validation.

To obtain grid-independent solutions, this paper created 5 sets of structured mesh through the commercial software ICEM. The boundary-layer settings of each mesh are the

same, and only the mesh size outside the boundary layer is changed. Figure 6 shows the effect of the node number on the discharge coefficient of the receiver holes. It can be seen from the figure that, when the number of the grid is more than 2.2×10^6 , the discharge coefficient of the receiver hole hardly changes. Therefore, the numerical results are no longer affected by the grid number when the number is more than 2.2×10^6 . The number of the grid used in the following is 2.2×10^6 .

As mentioned above, the turbulence model and mesh validation in this section were performed with the sector model (shown in Figure 4), while the full-loop model (shown in Figure 2) is used in the next section. So, it is necessary to confirm that the validated turbulence model and mesh setup parameters are also appropriate in the full-loop model. To verify the consistency of computation between the 360° domain and the $15^\circ/12^\circ$ domain, it is necessary to prove that the difference between the two kinds of domain is little. Figure 7 shows the distribution of the dimensionless static pressure near the stator along the radial direction calculated by the two models, which indicates that the deviation between the two domains is below 5% in most areas except the areas where the pressure is equal to that of the nozzles. Therefore, the validation of the turbulence model and mesh setting verified by the $15^\circ/12^\circ$ domain is also applicable to the 360° domain.

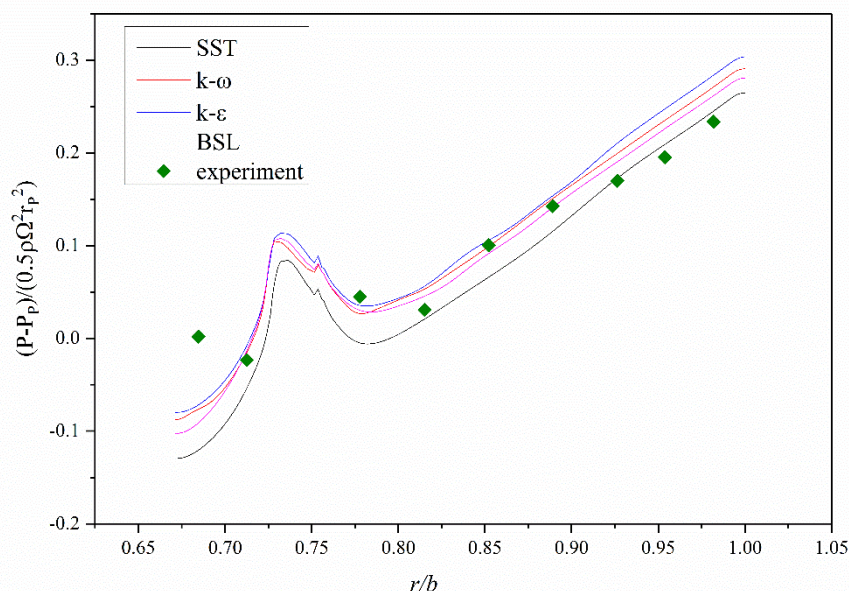


Figure 5. CFD static pressures at static disk versus experiment, $\lambda_{T,P} = 0.236$, $\beta_p = 0.96$.

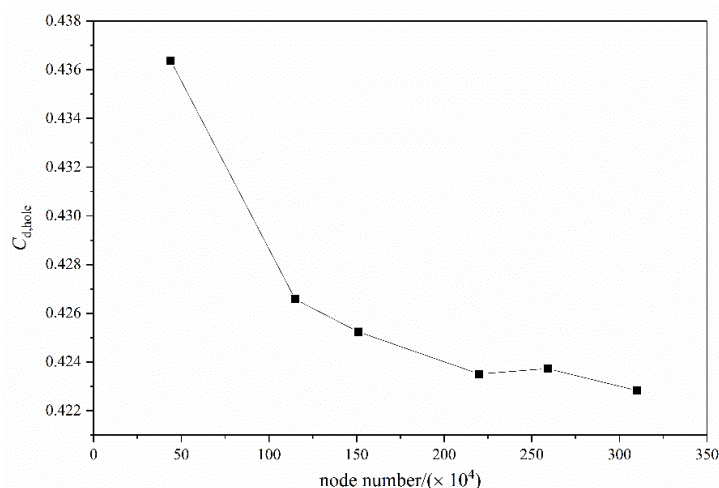


Figure 6. The grid-independent solution, $\lambda_{T,P} = 0.236$, $\beta_p = 0.96$.

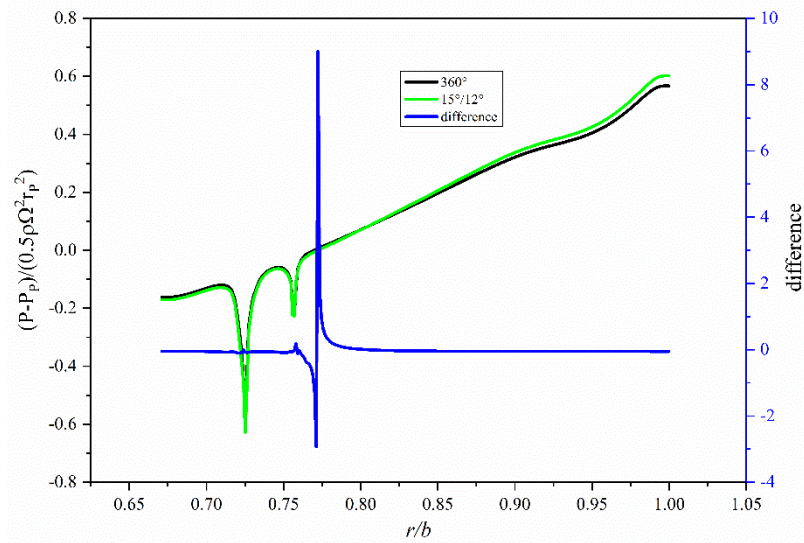


Figure 7. Profile of static pressure near stator for different models.

2.3. Definition of Parameters

This paper is mainly concerned with four dimensionless parameters, the definitions of which are specified below.

Mass flow ratio:

$$\eta_{hole_i} = \frac{m_{hole_i}}{m_{nozzle}/N_{hole}} \tag{1}$$

where m_{hole_i} is the mass flow rate of hole i (hole 0 is the receiver hole that corresponds to the fractured blade, and the other receiver holes are numbered as hole i ($i \neq 0$), with the direction of increasing i in the rotating direction.), m_{nozzle} is the inlet mass flow rate of the nozzles, and N_{hole} is the number of receiver holes. η_{hole_i} is used to describe the change in the mass flow rate of hole i after blade fracture compared to the average mass flow rate.

Total-pressure-loss efficiency:

$$C_{p,hole_i} = \frac{P_{nozzle,in,stn}^* + \frac{1}{2}\rho((\Omega r_{hole})^2 - V_{\phi,nozzle}^2) - P_{hole_i,out,stn}^*}{P_{nozzle,in,stn}^* - P_{hole_i,out}} \tag{2}$$

where $P_{nozzle,in,stn}^*$ is the total pressure of the nozzle inlet in the static frame, $P_{hole_i,out,stn}^*$ is the total pressure of the hole outlet in the static frame, and $P_{hole_i,out}$ is the static pressure of the hole outlet. $V_{\phi,nozzle}$ is the tangential velocity of the nozzle outlet, and $V_{\phi,nozzle} = m_{nozzle} \cos\alpha / \rho A_{nozzle}$. The definition of $C_{p,hole_i}$ refers to the work of the literature [26], which describes the pressure loss of the air as it travels from the nozzle to the hole i .

Discharge coefficient [2]:

$$C_{d,hole_i} = \frac{m_{hole_i}}{\frac{A_{hole} P_{hole_i,in,rel}^*}{\sqrt{RT_{hole_i,in,rel}^*}} \sqrt{\frac{2k}{k-1} \left(\left(\frac{P_{hole_i,out}}{P_{hole_i,in,rel}^*} \right)^{2/k} - \left(\frac{P_{hole_i,out}}{P_{hole_i,in,rel}^*} \right)^{1+1/k} \right)}} \tag{3}$$

The definition of $C_{d,hole_i}$ refers to the work of the literature [2], which describes the discharge coefficient of hole i . Where A_{hole} is the total area of the receiver holes, $P_{hole_i,in,rel}^*$ is the total pressure of the inlet of hole i in the relative frame, $T_{hole_i,in,rel}^*$ is the total temperature of the inlet of hole i in the relative frame, R is the ideal gas constant, and κ is the ratio of the specific heat of ideal gas.

Adiabatic effectiveness [2]:

$$\Theta_{ad,hole_i} = \frac{C_p(T_{nozzle,in,stn}^* - T_{hole_i,out,rel}^*)}{0.5\Omega^2 r_h^2} \quad (4)$$

$\Theta_{ad,hole_i}$ describes the adiabatic efficiency of the air as it travels from the nozzle to hole_i. The larger the value of Θ_{ad} , the lower the relative total temperature of the cold air entering the turbine blades, which means that the pre-swirl system has a better performance.

3. Results and Discussion

3.1. Influence of Pre-swirl Angle α

The distributions of η , C_p , C_d , and Θ_{ad} in the circumferential direction are shown in Figure 8, respectively, for different α . These curves all consist of 60 data points, each corresponding to a receiver hole. Hole_0, corresponding to the fractured blade, is located at 0° of the polar coordinate system, and hole_1 is located at 6° . The θ increases in the same direction as the rotation of the rotor (thus, hole_1 is located downstream of hole_0, whereas hole_59 is located upstream of it). This is also the same for the curves below and will not be repeated.

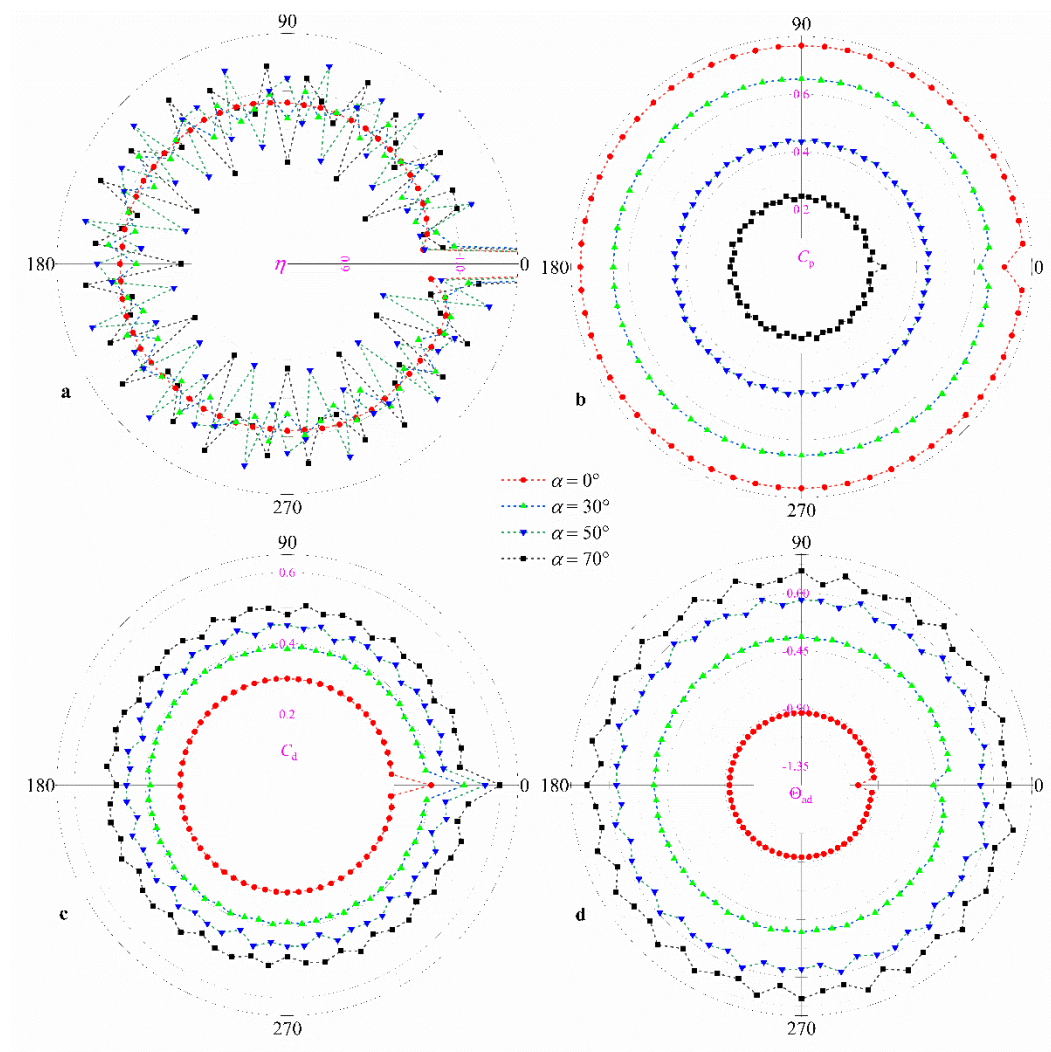


Figure 8. Distribution of (a) mass-flow-rate ratio η , (b) total-pressure-loss coefficient C_p , (c) discharge coefficient of holes C_d , and (d) adiabatic effectiveness Θ_{ad} for different pre-swirl angles α .

The distribution of mass flow is critical to the cooling of blades; so first, look at the distribution of η . Figure 8a shows the distribution of η for each receiver hole except hole_0. From the figure, it can be seen that the receiver holes around hole_0 are affected more by the fractured blade, while it has little influence on those holes far from hole_0. In addition, it is obvious from the figure that the amplitude of fluctuations gradually increases with the increase in α and shows a periodic character. It is important to note that the fluctuations in η are not due to the asymmetry of the boundary (blade fractured). As shown in Figure 9, even though the boundary conditions are symmetric (blade not fractured), the η of holes are still not equal. This indicates that the turbine blade fracture does not affect the area away from the fractured blade. This is supposed to be attributed to the method of Frozen Rotor and the reasons that will be described below. When $\alpha = 0^\circ$, the air is ejected from the nozzle and impacts the rotor vertically, and flows towards the high-radius region driven by the rotor. By the high-radius position, the flow tends to be uniform (as shown in Figure 10a, the vector is uniform near the receiver holes), and therefore η changes more smoothly. As α increases, the effect of the rotor on the air is reduced, resulting in the uneven flow caused by the discrete nozzles affecting the flow near the receiver hole (as shown in Figure 10a, the vector near the receiver holes is influenced by the nozzles). This is ultimately reflected in the fluctuations of η , so the period of the fluctuation is closely related to the number of nozzles.

As for hole_0, η_{hole_0} is 1.530, 1.527, 1.559, and 1.536 when α is 0° , 30° , 50° , and 70° , respectively. Considering the fluctuation in the mass flow rate between the holes, α has little effect on η_{hole_0} . Therefore, it can be understood that η_{hole_0} is larger at $\alpha = 50^\circ$ than at other values of α . That is because, when $\alpha = 50^\circ$, hole_0 is just near the crest of the fluctuation period. Of course, η_{hole_0} is also affected by fluctuations when α equals other values.

Figure 8b shows the distribution of C_p for each receiver hole. It is also clear from the figure that, when α is small, C_p is distributed relatively uniformly; as α increases, C_p gradually shows an obvious periodicity. The same law as the fluctuation in η , when α is small, the flow is only affected by the discrete nozzle in the low-radius region, while the high-radius region is homogenized by centrifugal force, so C_{p,hole_i} ($i \neq 0$) is equal except C_{p,hole_0} ; as α increases, the effect of the discrete nozzle gradually penetrates the high-radius region, so C_p gradually appears to fluctuate and shows a periodic pattern. Moreover, C_p decreases significantly with the increase in α . When $\alpha = 0^\circ$, the air flows outward radially near the stator in the low-radius region, while it is the radial inward flow near the stator in the high-radius region (as shown in Figure 11a). The mixing of these two parts of the air can cause large pressure losses. As α increases, the air impacts the rotor less and the mixing effect is also reduced (as shown in Figure 11c), so the pressure loss decreases.

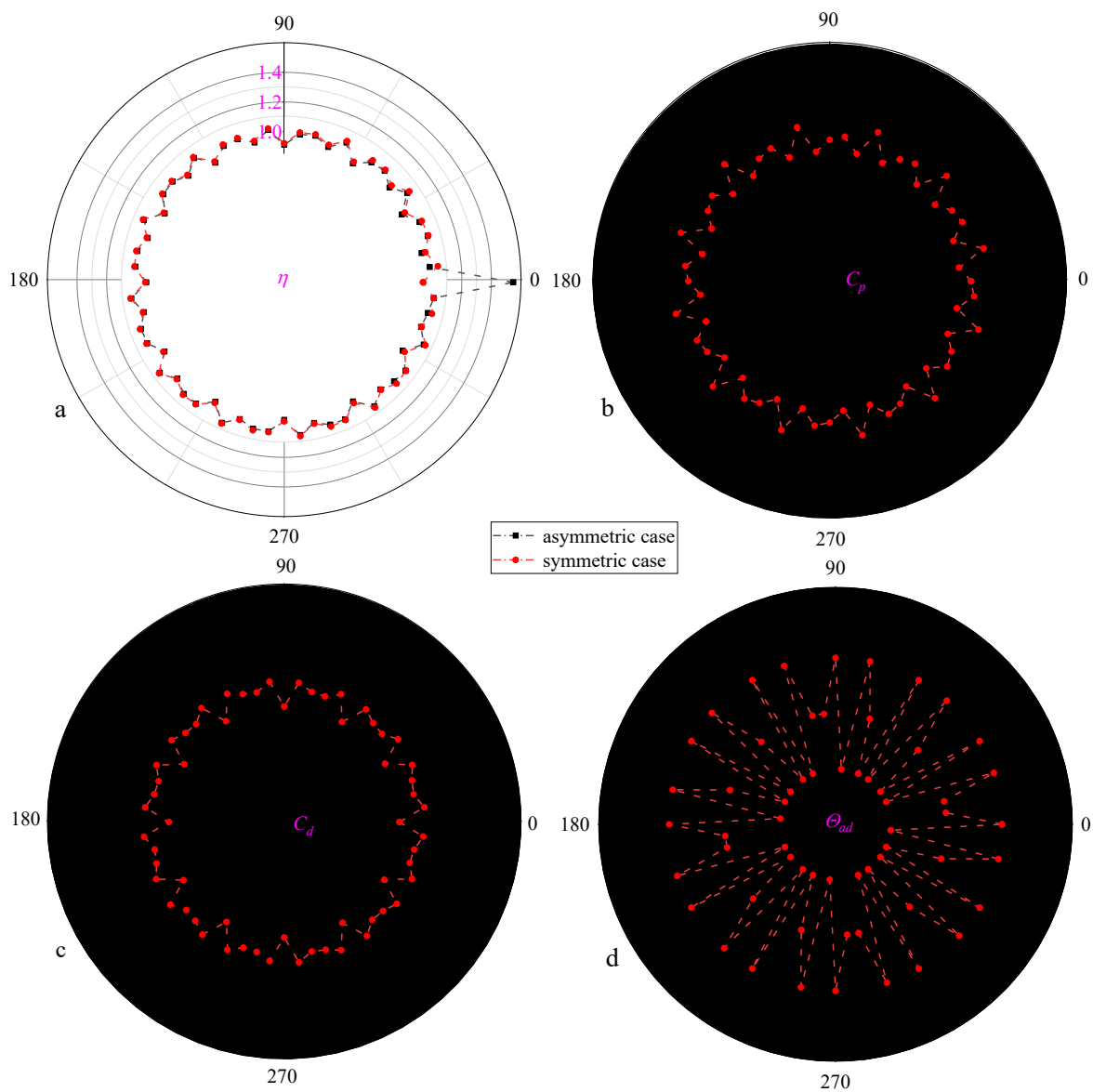


Figure 9. Distribution of (a) mass-flow-rate ratio η , (b) total-pressure-loss coefficient C_p , (c) discharge coefficient of holes C_d , and (d) adiabatic effectiveness Θ_{ad} for symmetric and asymmetric boundary conditions when $\alpha = 70^\circ$.

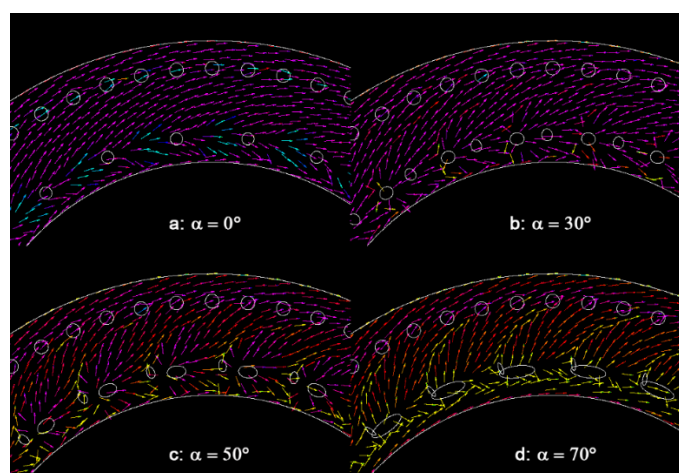


Figure 10. Vector at the plane $z = 0.5$ for different pre-swirl angles: (a) $\alpha = 0^\circ$, (b) $\alpha = 30^\circ$, (c) $\alpha = 50^\circ$, (d) $\alpha = 70^\circ$.

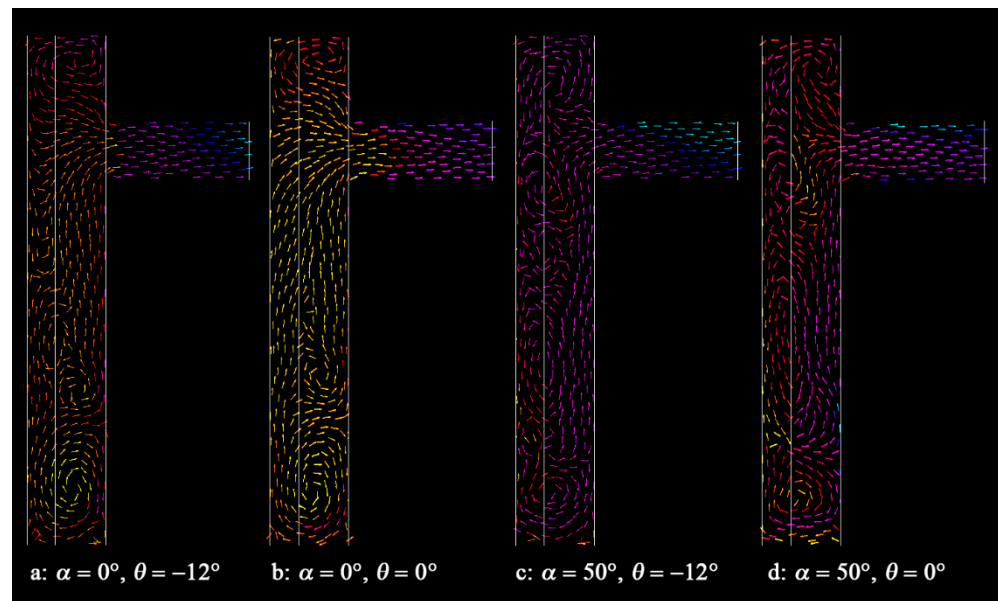


Figure 11. Vector at the r - z plane for $\alpha = 0^\circ$ and $\alpha = 50^\circ$.

As for hole_0, $C_{p,hole_0}$ is smaller than $C_{p,hole_i}$ ($i \neq 0$). Moreover, as α increases, the reduction rate of $C_{p,hole_0}$ compared with $C_{p,hole_i}$ ($i \neq 0$) decreases gradually. When increasing α to 70° , $C_{p,hole_0}$ even exceeds $C_{p,hole_i}$ ($i \neq 0$). When $\alpha = 0^\circ$, because the back pressure of hole_0 is lower than hole_i ($i \neq 0$), more air flows into hole_0, resulting in the mixing area near the stator almost disappearing (as shown in Figure 11b), so $C_{p,hole_0}$ is smaller than $C_{p,hole_i}$ ($i \neq 0$) instead. However, as α increases, the air enters the receiver hole through the rotor boundary layer and the inviscid core, but not through the stator boundary layer. Therefore, hole_0 does not affect the flow structure (as shown in Figure 11d) although its mass flow rate is higher, and the effect on the pressure loss is limited. Continuing to increase α , $C_{p,hole_0}$ instead exceeds $C_{p,hole_i}$ ($i \neq 0$); please refer to the next subsection for the reason.

Figure 8c shows the distribution of C_d of each receiver hole for different α . From the figure, it is obvious that C_d increases with increases in α . In general, the closer the β near the receiver hole is to 1, the larger the C_d of the receiver hole is [21]. As α increases, the β near the receiver hole also increases and gradually approaches 1, so C_d increases. Of course, the fluctuation in C_d increases with the increase in α for the same reason as η . Moreover, $C_{d,hole_0}$ is larger than $C_{d,hole_i}$ ($i \neq 0$) apparently, because the air inside hole_0 is more compressible. It is worth noting that, as α increases, the increase rate of $C_{d,hole_0}$ compared to $C_{d,hole_i}$ ($i \neq 0$) gradually decreases. The $C_{d,hole_0}$ is 34.7%, 27.7%, 24.5%, and 20.1% greater than the average of $C_{d,hole_i}$ ($i \neq 0$), when α is 0° , 30° , 50° , and 70° , respectively. This is mainly because the effect of the nozzles increases as α increases, while the effect of receiver holes relatively decreases.

Figure 8d shows the distribution of Θ_{ad} for different α . From the figure, it can be seen that Θ_{ad} increases significantly with the increase in α , while the fluctuation in Θ_{ad} also increases. According to Mahmood [27], Θ_{ad} is related to the β_p as well as the moment of stator:

$$\Theta_{ad} = 2\beta_p \left(\frac{r_{nozzle}}{r_{hole}} \right)^2 - 1 - \frac{M_s}{0.5m_{nozzle}\Omega r_{hole}^2} \quad (5)$$

As α increases, β_p increases significantly, while the moment of stator does not change much, so the Θ_{ad} increases. In addition, the $\Theta_{ad,hole_0}$ is smaller compared to $\Theta_{ad,hole_i}$ ($i \neq 0$). According to Equation (13) of the reference [27], the β near hole_0 is larger than that of the other receiver holes, thus leading to its smaller adiabatic efficiency. Meanwhile, it can be seen from the above that, when α is small (e.g., $\alpha = 0^\circ$), the influence of the receiver hole

on the flow is strong, leading to a large difference of Θ_{ad} between hole_0 and hole_i ($i \neq 0$); whereas, when α is large (e.g., $\alpha = 50^\circ/70^\circ$), the influence of the hole is relatively small, so the $\Theta_{ad,hole_0}$ is not much different from $\Theta_{ad,hole_i}$ ($i \neq 0$).

3.2. Influence of Area Ratio of Nozzles to Holes ξ

Figure 12a shows the distribution of η for each receiver hole (except hole_0) with different ξ . From the figure, it can be seen that as ξ increases from 0.156 to 0.625, the fluctuation amplitude of η gradually decreases or even disappears, and of course, the fluctuation shows a periodic pattern related to the nozzles. Continuing to increase ξ to 1.225, the η again shows some fluctuations, but mainly in the upstream of hole_0. When ξ is small, the β_p is larger, and thus the fluence of discrete nozzles is greater. Therefore, the distribution of η shows a clear periodic fluctuation closely related to the number of nozzles, and the fluctuation decreases as ξ increases. The unevenness caused by the nozzles diminishes, so the distribution tends to level off when ξ increases. Continuing to increase ξ to 1.225, the effect of the receiver holes becomes apparent, and the fluctuations in η in the upstream are due to fluctuations in C_d (shown in Figure 12c) and Coriolis force [18]. As for hole_0, η_{hole_0} is 1.711, 1.536, 1.532, and 1.543, when ξ is 0.156, 0.315, 0.625, and 1.225, respectively. Therefore, the effect of ξ on η_{hole_0} is minor considering the fluctuations.

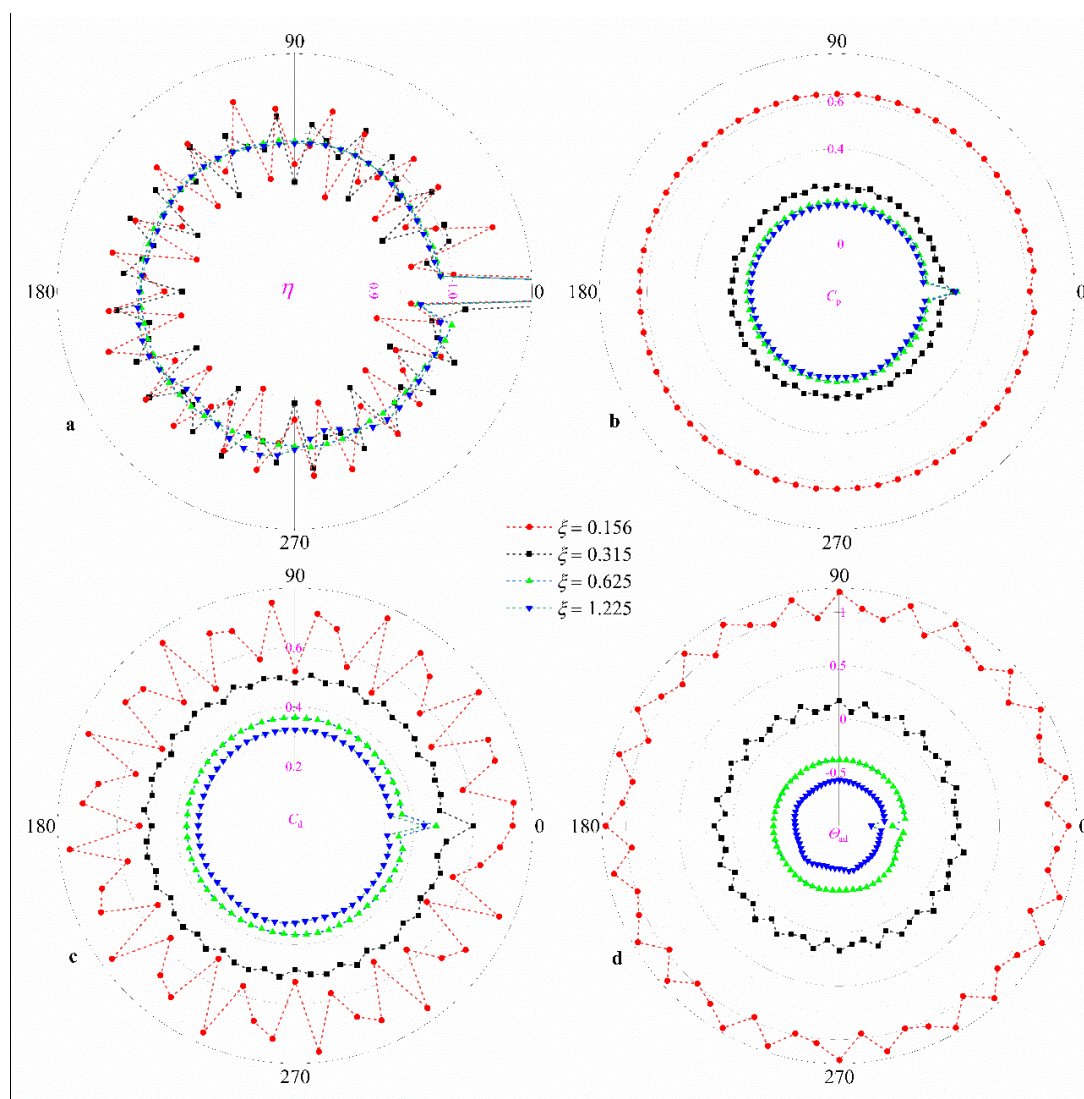


Figure 12. Distribution of (a) mass-flow-rate ratio η , (b) total-pressure-loss coefficient C_p , (c) discharge coefficient of holes C_d , and (d) adiabatic effectiveness Θ_{ad} for different area ratios of nozzles to holes ξ .

Figure 12b shows the distribution of C_p for each receiver hole with different ξ . From the figure, it can be seen that C_p decreases rapidly as ξ increases from 0.156 to 0.315; continuing to increase ξ , C_p still decreases, but the rate of decrease becomes slower. In general, pressure loss always occurs at the throat position. When $\xi = 0.156$, the pressure loss occurs mainly at the nozzle outlet. Moreover, at this time, the β_p is also very large (as shown in Figure 13a), resulting in work performed by the air to the rotor. Therefore, when $\xi = 0.156$, the C_p is large. When ξ increases from 0.156 to 0.315, the pressure loss of the nozzle decreases, and the work performed by the air on the rotor also changes to work performed by the rotor on the air, so C_p decreases rapidly. When ξ continues to increase, the pressure loss of the nozzle outlet continues to decrease, while the pressure loss in the cavity and receiver hole does not change much. Therefore, as ξ increases, C_p also decreases, but the rate of reduction slows down significantly.

Regarding hole_0, it is obvious from the figure that the $C_{p,hole_0}$ decreases and then increases with increasing ξ compared to $C_{p,hole_i}$ ($i \neq 0$), and the increase rate increases with increasing ξ . When $\xi = 0.156$, the β of the air is large, even exceeding the rotor. Due to the lower outlet pressure of hole_0, the air flows to hole_0 are smoother than hole_i ($i \neq 0$), and therefore $C_{p,hole_0}$ is lower than $C_{p,hole_i}$ ($i \neq 0$). When ξ is increased, the impact of air on the rotor is weakened, while the effect of the receiver hole becomes more and more significant. For example, when $\xi = 1.225$ (as shown in Figure 14), the mass flow rate of hole_0 increases more than the other receiver holes, which causes the radial velocity in some areas near the stator to become radially outward, and therefore the air mixing is stronger, so $C_{p,hole_0}$ is larger than $C_{p,hole_i}$ ($i \neq 0$), and the increase rate also increases with ξ .

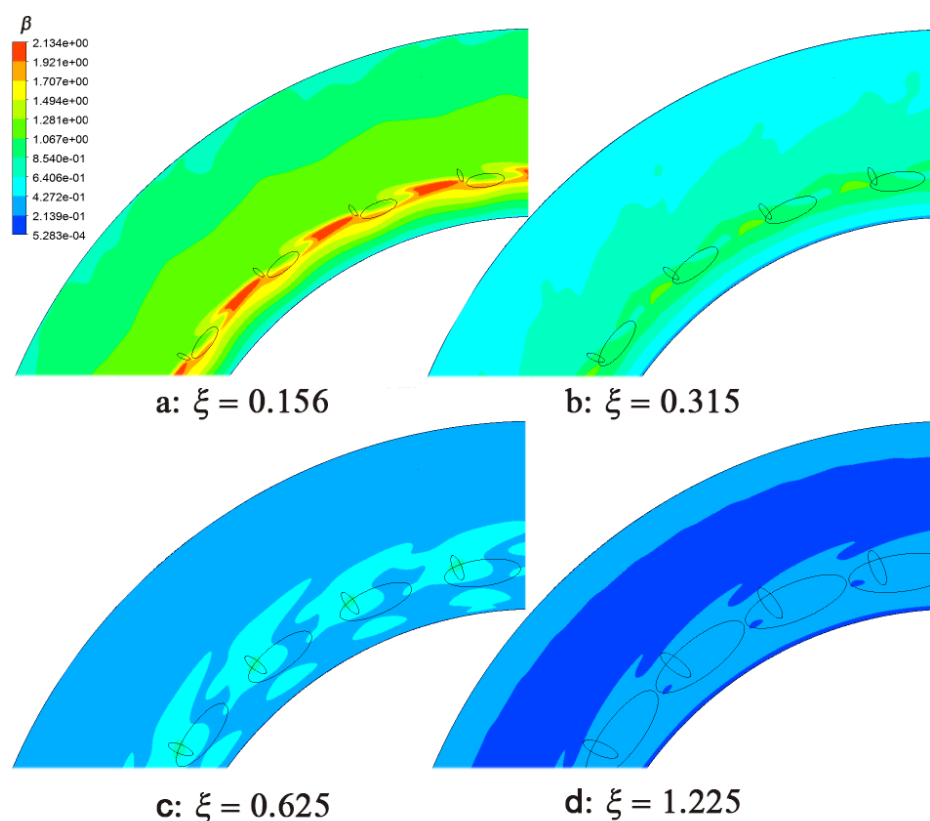


Figure 13. Contour of swirl ratio β at plane $z = 0.5$ for different area ratios of nozzles to holes: (a) $\xi = 0.156$, (b) $\xi = 0.315$, (c) $\xi = 0.625$, (d) $\xi = 1.225$.

Figure 12c,d shows the distribution of C_d and Θ_{ad} of each receiver hole with different ξ . It can be seen from the figure that, when ξ is small, the distribution of both has a more obvious periodic fluctuation pattern; as ξ increases, the receiver holes except hole_0 do

not differ much, and the distribution of C_d and Θ_{ad} are both more uniform. This is obviously due to the opposite effect of the nozzle and the receiver hole in different cases. Furthermore, as ξ increases, C_d and Θ_{ad} decrease. As for hole_0, the variation in C_d and Θ_{ad} relative to the other receiver holes increases with increasing ξ . This is because the influence of the nozzle decreases while the influence of the receiver hole increases.

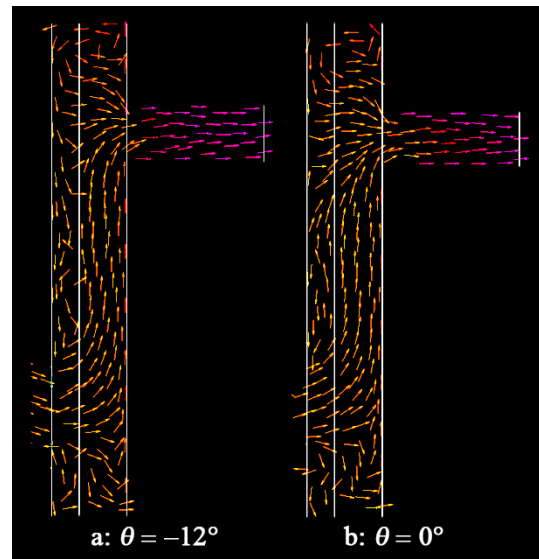


Figure 14. Streamlines at the r - z plane for $\xi = 1.225$: (a) $\theta = -12^\circ$, (b) $\theta = 0^\circ$.

3.3. Influence of Gap Ratio G

Figure 15a shows the distribution of η for each receiver hole (except hole_0) with different G . From the figure, it can be seen that the distribution of η shows a periodic pattern except for hole_0. Especially when $G = 0.0509$, the fluctuation amplitude is the largest. When G is small or larger, there are two vortices in low and high radius, and the flow structures are relatively stable (shown in Figure 16a and d, whose flow structures are not changed with θ). Only when G is of moderate size (e.g., $G = 0.0509$) does the transition area of the two vortices becomes unstable, and the relative position of the nozzle to the hole can affect its flow structure. For example, for $G = 0.0509$, the flow structures at the three tangential positions of $\theta = -24^\circ$ (shown in Figure 17a), $\theta = -18^\circ$ (shown in Figure 17b), and $\theta = -12^\circ$ (shown in Figure 16c) are not the same, which shows the instability of the flow structure. This results in large fluctuations in η . As for hole_0, η_{hole_0} is 1.545, 1.563, 1.536, and 1.556, when G is 0.0231, 0.0370, 0.0509, and 0.0648, respectively. The effect of G on η_{hole_0} is almost negligible.

Figure 15b shows the distribution of C_p for each receiver hole with different G . It is obvious from the figure that C_p decreases as G increases. When G is small, the air impacts the rotor, and the fluid in the cavity is strongly mixed, resulting in a large pressure loss. With the increase in G , the impact decreases and the pressure loss decreases. As for hole_0, C_{p,hole_0} is larger than C_{p,hole_i} ($i \neq 0$). Specifically, C_{p,hole_0} is 21.7%, 19.4%, 17.9%, and 17.1% larger than the average values of C_{p,hole_i} ($i \neq 0$), when G is 0.0231, 0.0370, 0.0509, and 0.0648, respectively. It can be seen that the increase rate of C_{p,hole_0} decreases slightly with increases in G . When $G = 0.0231$, the distance between rotor and stator is smaller. As more air flows to hole_0, it squeezes the space of the vortex in the cavity (as shown in Figure 18a), which causes some air to flow radially outward near the stator as well. This leads to more intense mixing near the stator, resulting in greater pressure loss. This phenomenon diminishes a lot as G increases, so the increase rate of C_{p,hole_0} decreases. When G continues to increase, the increase rate of C_{p,hole_0} seems to be gradually stabilized.

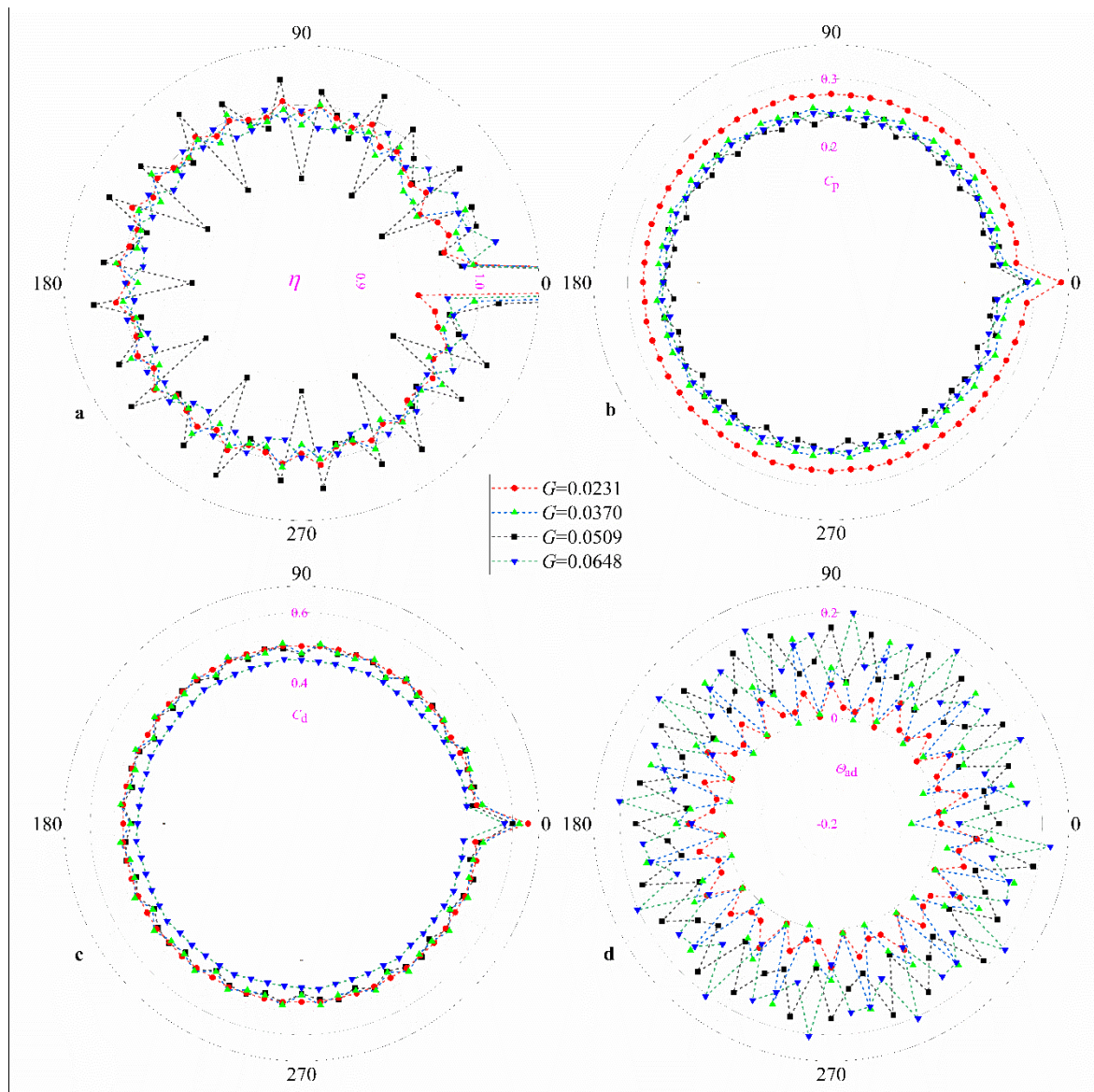


Figure 15. Distribution of (a) mass-flow-rate ratio η , (b) total-pressure-loss coefficient C_p , (c) discharge coefficient of holes C_d , and (d) adiabatic effectiveness θ_{ad} for different gap ratios G .

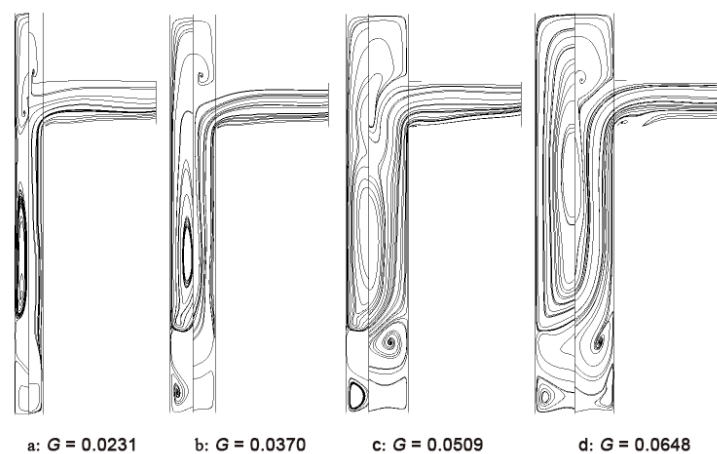


Figure 16. Streamline at plane $\theta = -12^\circ$ for different gap ratios: (a) $G = 0.0231$, (b) $G = 0.0370$, (c) $G = 0.0509$, (d) $G = 0.0648$.

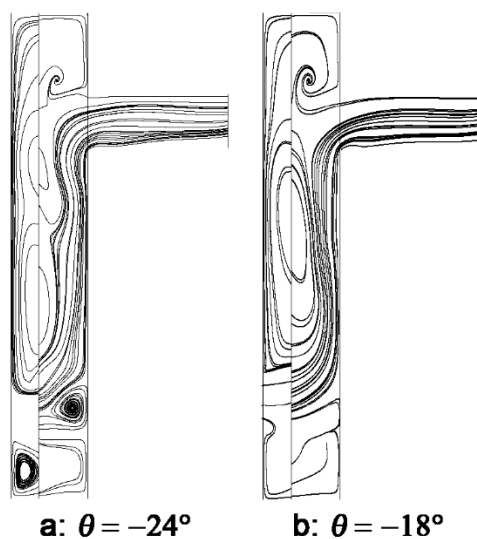


Figure 17. Streamlines at the z - r plane for $G = 0.0509$: (a) $\theta = -24^\circ$, (b) $\theta = -18^\circ$.

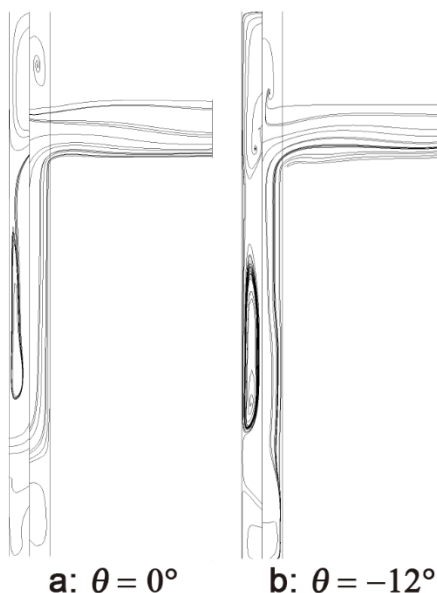


Figure 18. Streamlines at the z - r plane for $G = 0.0231$: (a) $\theta = 0^\circ$, (b) $\theta = -12^\circ$.

Figure 15c shows the distribution of C_d of each receiver hole with different G . As can be seen from the figure, C_d decreases as G increases. From Figure 19, it can be seen that as G increases, the β decreases, and therefore C_d decreases. In addition, $C_{d,hole_0}$ is significantly larger than $C_{d,hole_i}$ ($i \neq 0$), and the increase rate of $C_{d,hole_0}$ compared to $C_{d,hole_i}$ ($i \neq 0$) decreases with increases in G . Specifically, $C_{d,hole_0}$ increases by 27.5%, 23.2%, 20.1%, and 23.8%, respectively, compared to the average of $C_{d,hole_i}$ ($i \neq 0$) when G is 0.0231, 0.0370, 0.0509, and 0.0648. It can also be seen from Figure 19 that, for larger G , the difference of β between hole_0 and hole_i ($i \neq 0$) is small, and therefore the increase rate of $C_{d,hole_0}$ is relatively small. Another point worth noting is that C_d fluctuates with a middle G ($G = 0.037/0.0509$), while it is evenly distributed when G is small or large. This is the same law as the fluctuation in η . When G is in the middle position, the flow structure is relatively unstable, thus causing the fluctuation in C_d to show periodicity.

Figure 15d shows the distribution of Θ_{ad} for each receiver hole with different G . As can be seen from the figure, Θ_{ad} increases with increases in G . The change in G hardly affects the β_p but affects the moment of the stator. When G is small, the velocity gradient of the boundary layer is larger, and therefore the frictional moment is relatively large. The

effect of this friction reduces the Θ_{ad} , making the Θ_{ad} decrease. $\Theta_{ad,hole_0}$ is smaller than $\Theta_{ad,hole_i}$ ($i \neq 0$), but the reduction rate is significantly influenced by the distribution pattern of the Θ_{ad} .

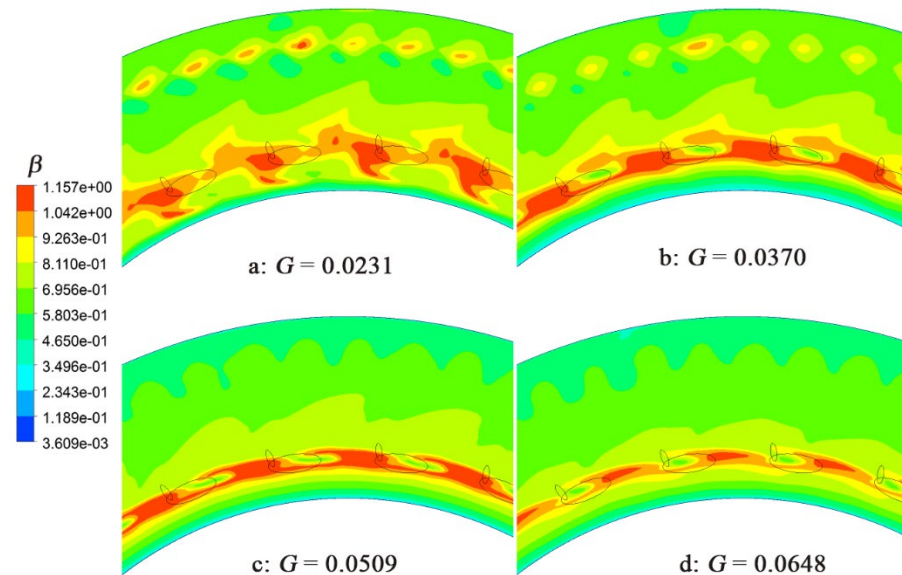


Figure 19. Contour of swirl ratio β at the plane $z = 0.5$ for different gap ratios: (a) $G = 0.0231$, (b) $G = 0.0370$, (c) $G = 0.0509$, (d) $G = 0.0648$.

3.4. Influence of Radius Ratio of Nozzles to Holes δ

Figure 20a shows the distribution of η for each receiver hole (except hole_0) for different δ . As can be seen from the figure, there are larger fluctuations when δ is closer to 1. This is because, when the difference in radial position between the nozzle and hole is large, the air flows along with the rotor to receiver holes, and the nozzle also has less influence. However, when the radial positions are closed, the air can be injected directly into the receiver holes. It is, therefore, more susceptible to discrete nozzles and exhibits greater fluctuations. The η_{hole_0} is 1.536, 1.695, 1.698, and 1.739 when δ is 0.8, 0.9, 1.0, and 1.05, respectively. It can be seen that the increase rate of η_{hole_0} compared to η_{hole_i} ($i \neq 0$) increases with increases in δ . Figure 21 shows the streamlines on a cylindrical surface of $r^* = 0.926$, from which it can be seen that, as δ increases, the air can flow directly into hole_0 (this is also supported by the study of Lewis et al. [6]), leading to a greater increase in η_{hole_0} .

Figure 20b shows the distribution of C_p of each receiver hole for different δ . From the figure, it can be seen that C_p increases with increases in δ . For the stator-rotor system with centrifugal through-flow, the pressure in the cavity is higher at the high-radius position than that at the low-radius position. Therefore, as δ increases, the total pressure of the nozzle inlet must increase (as shown in Figure 22). Moreover, the pressure at the outlet of the receiver hole is the same. Therefore, as δ increases, the C_p must also increase. As for hole_0, the increase in $C_{p,hole_0}$ compared to $C_{p,hole_i}$ ($i \neq 0$) decreases gradually with increases in δ . From the analysis above, it is clear that $C_{p,hole_0}$ is larger than $C_{p,hole_i}$ ($i \neq 0$) when δ is small. When δ is increased, the pressure loss of the nozzles also increases, while the pressure loss of the receiver hole does not change much, so $C_{p,hole_0}$ gradually equals $C_{p,hole_i}$ ($i \neq 0$). When δ is increased further (e.g., for $\delta = 1.05$), the flow separation at the inlet of hole_0 decreases significantly (as shown in Figure 21d), and therefore the $C_{p,hole_0}$ is smaller than $C_{p,hole_i}$ ($i \neq 0$).

Figure 20c shows the distribution of C_d of each receiver hole for different δ . It is obvious from the figure that C_d increases significantly with increases in δ , and the fluctuation amplitude also increases significantly. From Figure 23, it can be seen that the reason for

the increase in C_d is that the β has increased with the increase in δ . The increase in the fluctuation amplitude is because, when δ is larger, the air can be transmitted more directly to the receiver orifice, increasing the fluctuation amplitude. Of course, $C_{d,hole_0}$ is larger than $C_{d,hole_i}$ ($i \neq 0$).

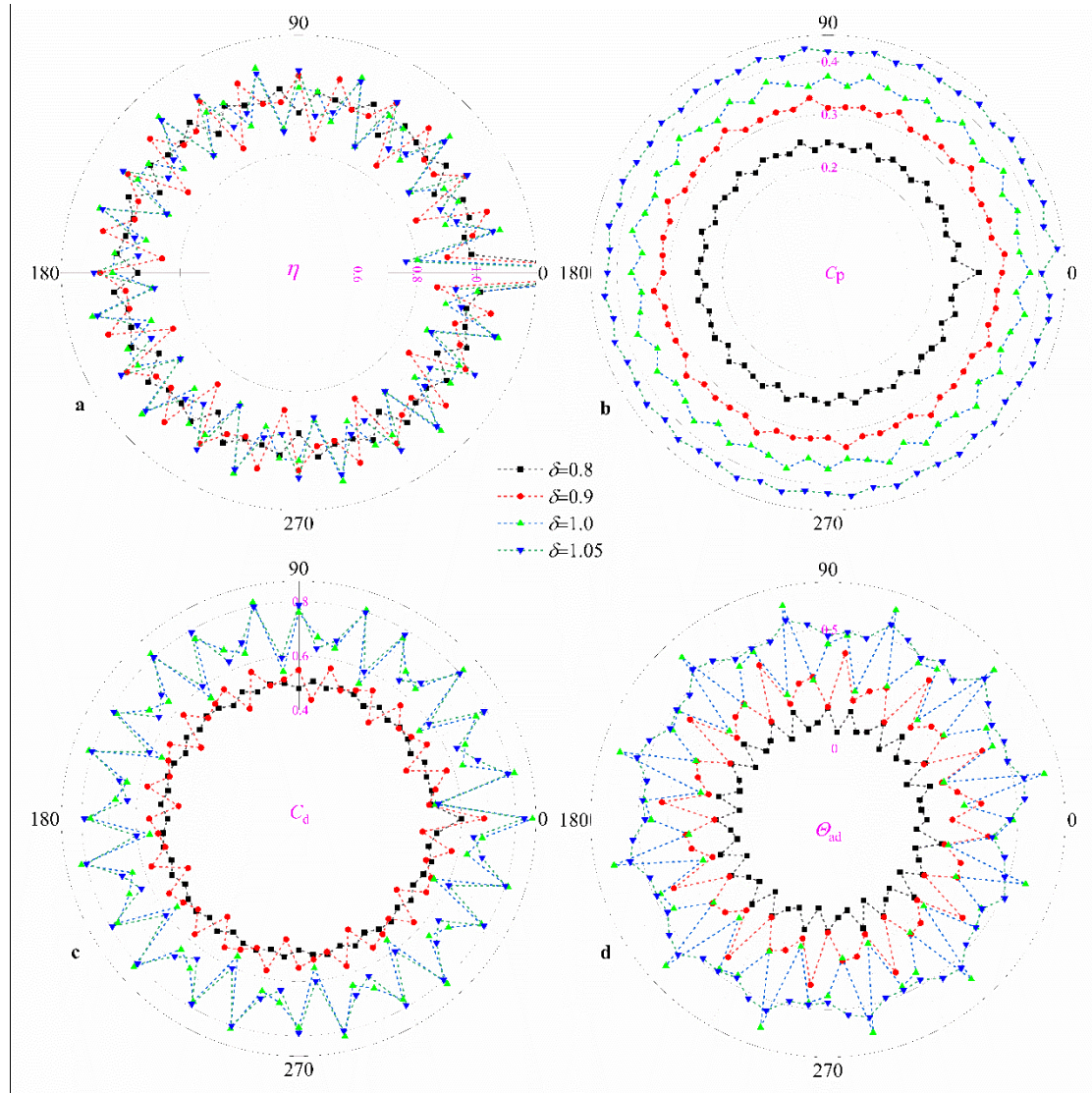


Figure 20. Distribution of (a) mass-flow-rate ratio η , (b) total-pressure-loss coefficient C_p , (c) discharge coefficient of holes C_d , and (d) adiabatic effectiveness Θ_{ad} for different radius ratios of nozzles to holes δ .

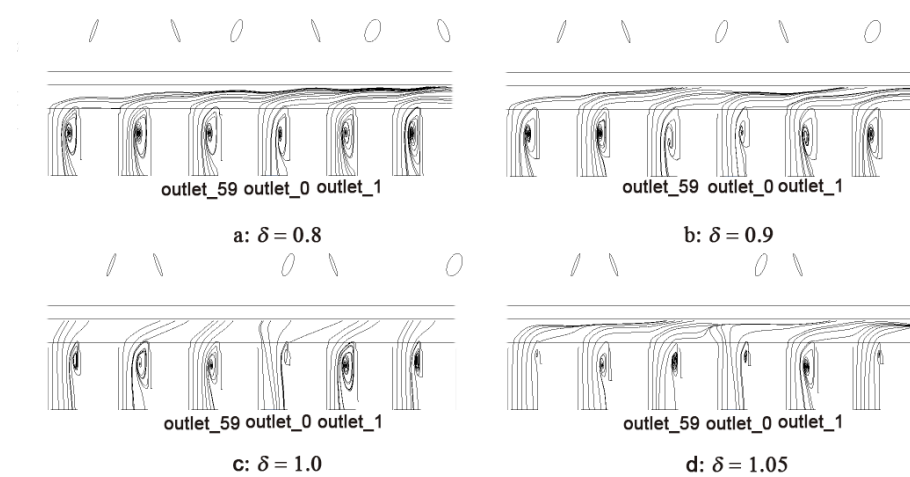


Figure 21. Streamlines at the cylindrical surface $r^* = 0.926$ for different radius ratios of nozzles to holes: (a) $\delta = 0.8$, (b) $\delta = 0.9$, (c) $\delta = 1.0$, (d) $\delta = 1.05$.

Figure 20d shows the distribution of Θ_{ad} of each receiver hole for different δ . It is obvious from the figure that Θ_{ad} increases with increases in δ . The change in the radius position of the nozzle does not affect the velocity of the nozzle outlet, so the tangential velocity of the nozzle outlet is the same. According to the theory of Mahmood [27], the value of the first term of Equation (5) increases with increases in δ , but the moment of stator does not change much. Therefore, as δ increases, Θ_{ad} increases. Of course, when $\delta = 1.0$, the fluctuation amplitude of Θ_{ad} is the highest. It is because at this time the distance between the nozzle and the receiver hole is the closest, and the nozzle has the greatest impact on Θ_{ad} .

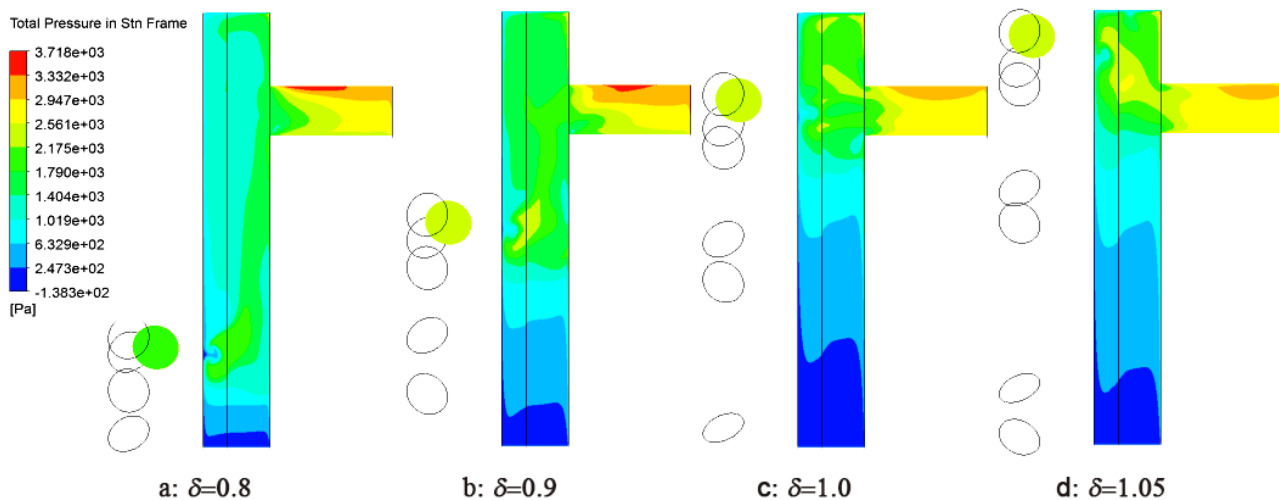


Figure 22. Contour of total pressure in the static frame at plane $\theta = -12^\circ$ for different radius ratios of nozzles to holes: (a) $\delta = 0.8$, (b) $\delta = 0.9$, (c) $\delta = 1.0$, (d) $\delta = 1.05$.

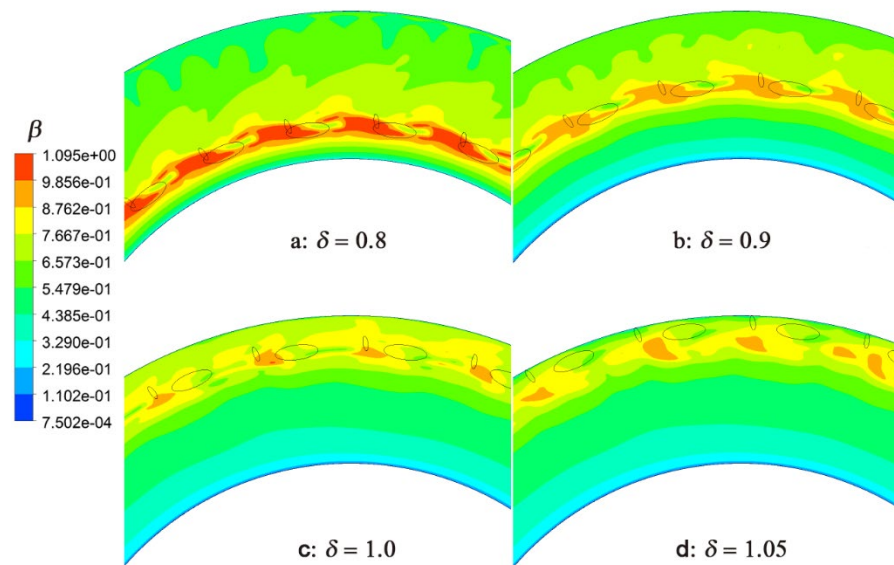


Figure 23. Contour of swirl ratio β at the plane $z = 0.5$ for different radius ratios of nozzles to holes: (a) $\delta = 0.8$, (b) $\delta = 0.9$, (c) $\delta = 1.0$, (d) $\delta = 1.05$.

4. Conclusions

The effect of blade fracture on the pre-swirl system is an issue that must be studied because it may affect the safety of the engine. Therefore, this paper investigates the effects of the pre-swirl angle, α ; area ratio of nozzles and holes, ξ ; gap ratio, G ; and radius ratio of nozzle and hole, δ , of a pre-swirl stator-rotor system on the mass-flow-rate ratio, η ; total-pressure-loss coefficient, C_p ; discharge coefficient of holes, C_d ; and adiabatic effectiveness, Θ_{ad} , which are investigated by numerical simulation with a single blade fractured. Through the above work, this paper attempts to answer which geometric parameter changes have a minor impact on the flow of a pre-swirl system after turbine blade fracture and to provide the basis and ideas for the passive safety design of the system. Within the scope of this paper's study, the following conclusions can be drawn from the above analysis:

- (1) As far as the distribution of η , the η of hole_0 (hole_0 is the receiver hole that corresponds to the fractured blade), η_{hole_0} , will be larger than that of hole_i ($i \neq 0$), η_{hole_i} . Furthermore, most of the geometric parameter changes do not increase η_{hole_0} . However, measures to increase the influence of the pre-swirl nozzles can reduce the influence of the blade fracture on mass flow distribution, such as larger α , smaller ξ , and larger δ .
- (2) As for C_p , C_d , and Θ_{ad} , α and ξ have a greater impact on it. For example, the C_d of receiver holes far from hole_0 decreases by over 70% when α increases from 0° to 70° . Of course, similar to η , increasing the influence of the pre-swirl nozzles can reduce the difference of C_p , C_d , and Θ_{ad} between receiver holes. Moreover, taking α for an example, the $C_{d,hole_0}$ is 34.7%, 27.7%, 24.5%, and 20.1% greater than the average of $C_{d,hole_i}$ ($i \neq 0$), when α is 0° , 30° , 50° , and 70° , respectively.
- (3) For the pre-swirl system, the structure that minimizes the change in cold-air conditions (it is better to include all four parameters) for different receiver holes when the turbine blades fracture is the best design. From this perspective, increasing the influence of the pre-swirl nozzle seems to be a better design, for example, by increasing α , or decreasing ξ . However, although increasing the effect of the nozzle serves the purpose, it increases the volatility of the flow. From the investigation of other researchers, the pre-swirl nozzle of the leaf grille type should be able to mitigate the fluctuation in the flow.

Author Contributions: Funding acquisition, T.Q. and P.L.; writing—original draft, G.Z. All authors have read and agreed to the published version of the manuscript.

Funding: This research was funded by the Project of National Science Foundation of China, grant number 61890923. The APC was funded by the Project of National Science Foundation of China No. 61890923.

Data Availability Statement: Not applicable.

Acknowledgments: The authors express their sincere gratitude to the support of the National Fund.

Conflicts of Interest: The authors declare no conflict of interest.

Abbreviations

Alphabet

a	inlet radius, m
A	area, m ²
b	radius of rotor and stator, m
C_p	total-pressure-loss coefficient
C_d	discharge coefficient
C_w	dimensionless mass flow rate, $m_{nozzle}/\mu b$
s	axial spacing between rotor and stator, m
T^*	total temperature, K
E	Euler number, $(P_2-P_1)/0.5\rho\Omega^2b^2$
G	gap ratio, s/b
m	mass flow rate, kg/s
N	number of nozzles or receiver holes
P	static pressure, Pa
P^*	total pressure, Pa
r^*	dimensionless radius, r/b
r_h	radius of receiver hole, m
r_p	radius of pre-swirl nozzle
z^*	dimensionless axial location, z/a
Re_φ	rotational Reynolds number, $\Omega b^2/\nu$
V_r, V_φ	radial and tangential velocity, m/s

Greeks

α	pre-swirl angle, degree
β	swirl ratio, $V_\varphi/\Omega r$
β_p	pre-swirl ratio, $V_{\varphi, nozzle, out}/\Omega r_p$
θ	axes of polar coordinates, degree
ξ	area ratio of nozzles and receiver holes, A_{nozzle}/A_{hole}
δ	radial location ratio of nozzles and receiver holes, r_p/r_h
η	mass-flow ratio, $m_{hole_i}/(m_{nozzle}/N_{hole})$
Ω	rotating velocity of the rotor, rad/s
ν	kinematic viscosity, m ² /s
ρ	density, kg/m ³
λ_T	turbulent flow parameter, $C_w/Re_\varphi^{0.8}$
Θ_{ad}	adiabatic effectiveness

Subscript

r, z, φ	radial, axial, and tangential coordinates
nozzle	pre-swirl nozzle
hole	receiver hole
stn	in the frame of static
rel	in the frame of relative
hole_i	receiver hole numbered i
p	pre-swirl nozzle
h	receiver hole

References

1. Lee, J.; Lee, H.; Kim, D.; Cho, J. The effect of rotating receiver hole shape on a gas turbine pre-swirl system. *J. Mech. Sci. Technol.* **2020**, *34*, 2179–2187. <https://doi.org/10.1007/s12206-020-0439-2>.
2. Zhang, F.; Wang, X.J.; Li, J. Numerical investigation of flow and heat transfer characteristics in radial pre-swirl system with different pre-swirl nozzle angles. *Int. J. Heat Mass Tran.* **2016**, *95*, 984–995. <https://doi.org/10.1016/j.ijheatmasstransfer.2016.01.010>.
3. Zhang, F.; Wang, X.J.; Li, J. Numerical investigation on the flow and heat transfer characteristics in radial pre-swirl system with different fillet radius at the junction of inlet cavity and nozzle. *Appl. Therm. Eng.* **2016**, *106*, 1165–1175. <https://doi.org/10.1016/j.applthermaleng.2016.06.117>.
4. Zhang, F.; Wang, X.; Liao, G.; Li, J. Computational fluid dynamics analysis for effect of length to diameter ratio of nozzles on performance of pre-swirl systems. *Proc. Inst. Mech. Eng. Part A J. Power Energy* **2015**, *229*, 381–392.
5. Zhao, G.; Ding, S.; Qiu, T.; Zhang, S. Numerical Investigation of the Effect of an Axial Pre-Swirl Nozzle With a Radial Angle in a Pre-Swirl Rotor-Stator System. In Proceedings of the Turbo Expo: Power for Land, Sea, and Air, Virtual, 7–11 June 2021; p. V05BT14A016.
6. Lewis, P.; Wilson, M.; Lock, G.D.; Owen, J.M. Effect of radial location of nozzles on performance of preswirl systems: A computational and theoretical study. *Proc. Inst. Mech. Eng. Part A J. Power Energy* **2009**, *223*, 179–190. <https://doi.org/10.1243/09576509jpe689>.
7. Kakade, V.U.; Lock, G.D.; Wilson, M.; Owen, J.M.; Mayhew, J.E. Effect of radial location of nozzles on heat transfer in preswirl cooling systems. *J. Turbomach.* **2011**, *133*, 1051–1060.
8. Lee, H.; Lee, J.; Kim, D.; Cho, J. Optimization of pre-swirl nozzle shape and radial location to increase discharge coefficient and temperature drop. *J. Mech. Sci. Technol.* **2019**, *33*, 4855–4866. <https://doi.org/10.1007/s12206-019-0926-5>.
9. Kong, X.; Huang, T.; Liu, Y.; Chen, H.; Lu, H. Effects of pre-swirl radius on cooling performance of a rotor-stator pre-swirl system in gas turbine engines. *Case Stud. Therm. Eng.* **2022**, *37* 102250.
10. Meher-Homji, C.B. Blading vibration and failures in gas turbines: Part A—Blading dynamics and the operating environment. In Proceedings of the ASME 1995 International Gas Turbine and Aeroengine Congress and Exposition, Houston, TX, USA, 5–8 June 1995; pp. 1–11.
11. Bureau, A.T.S. *Power Plant Failures in Turbofan-Powered Aircraft 2008 to 2012*; AR-2013-002; Australian Transport Safety Bureau: Canberra, Australia, 19 June 2014; pp. 1–34.
12. Bureau, A.T.S. *Power Plant Failures in Turbofan-Powered Aircraft 2012 to 2016*; Australian Transport Safety Bureau: Canberra, Australian, 2017.
13. Administration, F.A. *Airworthiness Standards: AIRCRAFT Engines: 33.75 Safety Analysis*; Federal Aviation Administration: Washington, DC, USA, 2009; Volume e-CFR 14 part 33.
14. Bein, M.; Shavit, A.; Solan, A. Nonaxisymmetric flow in the narrow gap between a rotating and a stationary disk. *J. Fluids Eng.* **1976**, *98*, 217–223.
15. Bein, M.; Shavit, A. Nonaxisymmetric Flow in the Narrow Gap Between a Rotating and a Stationary Disk with an Eccentric Source. *J. Fluid Eng.* **1977**, *99*, 418–421.
16. Mukhopadhyay, A.; Banerjee, S.; Gupta, C. Fully developed hydrodynamic and thermal transport in combined pressure and electrokinetically driven flow in a microchannel with asymmetric boundary conditions. *Int. J. Heat Mass Tran.* **2009**, *52*, 2145–2154. <https://doi.org/10.1016/j.ijheatmasstransfer.2008.08.035>.
17. Chan, Y.; Chen, G.; Tso, C. Effect of asymmetric boundary conditions on Couette–Poiseuille flow of power-law fluid. *J. Thermophys. Heat Tr.* **2015**, *29*, 496–503.
18. Zhao, G.; Qiu, T.; Liu, P. Influence of blade fracture on the flow of rotor-stator systems with centrifugal superposed flow. *Aerospace* **2022**, *9*, 106. <https://doi.org/10.3390/Aerospace9020106>.
19. Owen, J.M.; Rogers, R.H. *Flow and Heat Transfer in Rotating Disc Systems: Rotor-Stator Systems*, 5 ed.; LTD., R.s.p., Ed.; Research Studies Press LTD.: Somerset, UK, 1989; Volume 90, p. 278.
20. Lock, G.D.; Yan, Y.Y.; Newton, P.J.; Wilson, M.; Owen, J.M. Heat transfer measurements using liquid crystals in a preswirl rotating-disk system. *J. Eng. Gas Turbines. Power-Trans. Asme* **2005**, *127*, 375–382. <https://doi.org/10.1115/1.1787509>.
21. Lock, G.D.; Wilson, M.; Owen, J.M. Influence of fluid dynamics on heat transfer in a preswirl rotating-disk system. *J. Eng Gas Turbines Power-Trans Asme* **2005**, *127*, 791–797. <https://doi.org/10.1115/1.1924721>.
22. Kakade, V.U.; Lock, G.D.; Wilson, M.; Owen, J.M.; Mayhew, J.E. Accurate heat transfer measurements using thermochromic liquid crystal. Part 2: Application to a rotating disc. *Int. J. Heat Fluid Flow* **2009**, *30*, 950–959.
23. Yan, Y.; Gord, M.F.; Lock, G.D.; Wilson, M.; Owen, J.M. Fluid dynamics of a pre-swirl rotor-stator system. *J. Turbomach.* **2003**, *125*, 641–647. <https://doi.org/10.1115/1.1578502>.
24. Kamahl, J.; von Wolfersdorf, J.; Tham, K.M.; Wilson, M.; Lock, G. Computational fluid dynamics simulations of flow and heat transfer in a preswirl system: Influence of rotating-stationary domain interface. *J. Eng. Gas Turbines Power-Trans. Asme* **2012**, *134*, 052502. <https://doi.org/10.1115/1.4004730>.
25. Liao, G.; Wang, X.; Li, J. Numerical investigation of the pre-swirl rotor-stator system of the first stage in gas turbine. *Appl. Therm. Eng.* **2014**, *73*, 940–952.

-
26. Luo, X.; Han, G.; Wu, H.; Wang, L.; Xu, G. Experimental investigation of pressure loss and heat transfer in a rotor–stator cavity with two outlets. *Int. J. Heat Mass Tran.* **2014**, *78*, 311–320.
 27. Farzaneh-Gord, M.; Wilson, M.; Owen, J.M. Numerical and theoretical study of flow and heat transfer in a pre-swirl rotor-stator system. In Proceedings of the ASME Turbo Expo 2005, Vol 6, Pts A and B. Reno, NV, USA, 2005; pp. 943–949.